M&C 2017 - International Conference on Mathematics & Computational Methods Applied to Nuclear Science & Engineering, Jeju, Korea, April 16-20, 2017

Spectral X-ray Radiography for Safeguards at Nuclear Fuel Fabrication Facilities: A Feasibility Study

Andrew J. Gilbert*, Benjamin S. McDonald, L. Eric Smith

Pacific Northwest National Laboratory, Richland, WA 99354, United States
**andrew.gilbert@pnnl.gov*

Abstract - *Accurate, noninvasive accounting of total uranium and uranium-235 concentration at fuel fabrication facilities continues to present a challenging research problem. The methods used by the International Atomic Energy Agency are time consuming and require in-field chemistry, with operation by experts. Spectral X-ray radiography, along with advanced inverse algorithms, is an alternative measurement that could be completed noninvasively, without any in-field chemistry, and with verification measurements completed in minutes. The proposed measurement system and algorithms are presented here for the quantification of total uranium mass. The inverse algorithm uses total variation regularization and adaptive regularization parameter selection with the unbiased predictive risk estimator. Performance of the system is quantified with simulated X-ray data and sensitivity of the output is tested against various measurement system instabilities as well as inhomogeneities in the fuel powder density. Initial findings on the achievable accuracy and precision of this spectral X-ray method indicate strong potential to meet or exceed IAEA's targets for quantification of uranium oxide samples in the field.*

I. INTRODUCTION

The in-field verification measurement technology used by the International Atomic Energy Agency (IAEA) to ensure accurate accounting of nuclear material at fuel fabrication facilities is typically the Combined Procedure for Uranium Concentration and Enrichment Assay (COMPUCEA) [1]. Hybrid K-Edge Densitometry (HKED) is another technique in use by the IAEA, which can measure uranium concentration in samples, but is typically used in reprocessing plants and is installed in a facility permanently. [2]. These methods determine uranium concentration by observing the X-ray transmission around the L- and K-edge of the X-ray attenuation coefficients, respectively, and both result in the destruction of the samples via a chemical preparation process. These methods require carefully controlled dissolution chemistry and time-intensive data acquisition on the order of 1000s of seconds. A field-deployable technology that can accurately and nondestructively determine both total uranium mass and uranium-235 relative concentration, while reducing data acquisition times by an order of magnitude, would significantly improve the efficiency and reduce the complexity of IAEA safeguards approaches at fuel fabrication facilities. Pacific Northwest National Laboratory is exploring the viability of spectral X-ray radiography techniques, based on measurement of the transmitted X-ray spectrum, to meet this challenge in international safeguards.

In prior work not related to the uranium oxide assay application, inverse algorithms for X-ray material discrimination were developed for use with data from high-rate spectral X-ray radiography detectors. This was pursued to explore how multi-modal imaging (images that yield structure and material composition data) might be useful as attributes or in templates in an arms control verification context [3]. The key development in the previous work was development of an efficient, robust, and adaptive inverse algorithm to determine material composition from data obtained from spectral X-ray detectors. The algorithms developed showed excellent performance in discriminating and quantifying high-atomic-numbered materials even in layered configurations [4]. Performance was found to be particularly good when the object contained only three or four expected materials, consistent with what would be expected in encapsulated fuel powder verification measurements at nuclear fuel fabrication facilities. Of particular importance was the development of a method to optimally select a parameter in the algorithm that results in accurate material estimations [4]. The adaptive nature of these algorithms could be valuable for IAEA deployed systems since they wouldn't require expert operators. This is a key improvement over the COMPUCEA and HKED systems, which require operation by expert technicians or inspectors.

Here, we present a model-based feasibility study of the application of inverse algorithms to the noninvasive quantification of total uranium content in fuel powders at fuel fabrication facilities. Spectral X-ray assay was simulated in MCNP [5] and assumes a nominal detector response for a cadmium telluride X-ray detector. The inverse algorithms were applied to the simulated data to determine quantities of uranium (U), oxygen (O), and gadolinium (Gd) noninvasively. We show that material parameters (i.e., mass of select elements) determined from these preliminary explorations exhibit levels of uncertainty similar to those provided by today's IAEA methods in the field. In order to test the robustness of the algorithm to realistic instabilities in a deployed verification measurement system, the sensitivity of the material estimations to expected measurement system variations was determined.

II. METHODS

The response of a spectral transmission X-ray system to an arbitrary object can be described using a modified form of Beer's law, paired with a detector response model $S(E)$ [6]:

$$d(\boldsymbol{\rho}, E_{bin,\ell}) = \int_0^\infty S_\ell(E)\phi_0(E)\exp\left[-\sum_k \mu_k(E)\rho_k\right]\mathrm{d}E. \quad (1)$$

Here, d is the detector output for an energy bin ℓ and S_ℓ is the energy-dependent bin sensitivity of energy bin ℓ. The X-ray flux at the image plane is ϕ, ϕ_0 is the unattenuated flux, μ_k is the mass attenuation coefficient of the k'th material and ρ_k is its areal density in a given pixel. The density vector $\boldsymbol{\rho}$ indicates that the transmitted flux depends on a vector of any number of materials between the X-ray source and the detector.

From Eq. (1), known assay-system parameters, and sample material composition, an expected output from a spectral X-ray radiography system can be calculated. This is the forward problem. The inverse problem is to determine the material composition from the data output of the radiography system. For a typical problem, this can be done using simple least-squares fitting. However, since the material attenuation coefficients are not strongly unique (other than around the K-edges), e.g., Fig. 2, it has been shown that least-squares solutions are quite sensitive to image data noise. Therefore, regularization was required to accurately determine material composition [4] by minimizing the cost function $F(\boldsymbol{\rho})$.

$$F(\boldsymbol{\rho}) = \frac{1}{2}\left\| \frac{\boldsymbol{d}_n(\boldsymbol{\rho}) - \boldsymbol{d}_{obs}}{\sqrt{\boldsymbol{d}_{n-1}(\boldsymbol{\rho})}} \right\|^2 + \alpha \sum \sqrt{(\mathbf{D_i}\boldsymbol{\rho})^2 + (\mathbf{D_j}\boldsymbol{\rho})^2 + \beta}. \tag{2}$$

Here, the first, least-squares term comparing the modeled detector output $\boldsymbol{d}(\boldsymbol{\rho})$ to the observed data $\boldsymbol{d}_{obs}$ was normalized by the square root of the forward problem calculation from the previous iteration, $n-1$. This was done so that the variance in the high-count (e.g., background) pixel data does not overweight the norm, and to simplify the regularization parameter α selection method. The density vector $\boldsymbol{\rho}$ was expanded to include all materials of interest for all image pixels. Accordingly, the vector $\boldsymbol{d}$ contains the data for all detector pixels and energy bins. The minimization of F was done over this entire vector.

The second term was the total variation regularization, which smooths the solution by penalizing for sharp variations between neighboring pixels. This was weighted by α, which varies the strength of the regularization. The operator matrices $\mathbf{D_i}$ and $\mathbf{D_j}$ determine the backwards finite difference of the $\boldsymbol{\rho}$ vector in the row i and column j dimension of the image data, respectively [7]. These operator matrices were defined so that the variation across image borders or between the different materials is not taken into account in the calculation of the total variation. The term β ensures that the function is differentiable so that analytical first and second derivatives can be found for optimization. This term was set to unity in this study.

The minimum of Eq. (2) was found using the Gauss-Newton algorithm, with the application of a non-negativity constraint using the projected gradient, reduced Hessian algorithm [8]. The Gauss-Newton algorithm is iterative and approximates F as quadratic at each iteration and minimizes that approximation. To accomplish this, the first derivative (gradient) and second derivative (Hessian), or an approximation thereof, is required. The Gauss Newton algorithm uses the Jacobian of the misfit term to approximate its second derivative H, i.e., $H \approx J^T J$. Though Newton-type algorithms are not resistant to falling into local minima, it was found this wasn't a problem in practice.

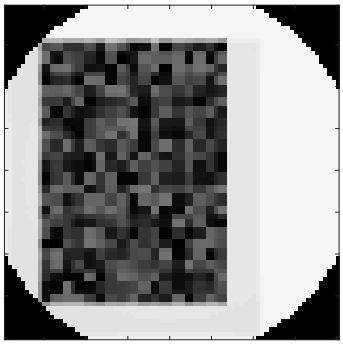

Fig. 1: A simulated X-ray radiograph of an inhomogenuous fuel powder geometry being inspected ($\log_{10}$-transformed), for the 100-117 keV energy window on a cadmium telluride detector. The corners of the radiograph are dark due to the extent of the conical X-ray beam.

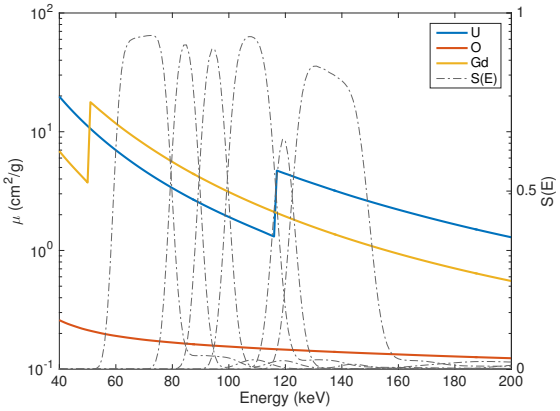

Fig. 2: The simulated CdTe detector response and attenuation coefficients used in the modeling study for fuel powder assay. The attenuation coefficients (left axis) are given as solid, colored lines while the detector response of a simulated 5-mm thick CdTe detector (right axis) is shown as dashed, gray lines.

The value for α was selected adaptively within the optimization algorithm using the unbiased predictive risk estimator (UPRE) method, as in [4]. The predictive risk $\boldsymbol{p}_\alpha$ is defined as

$$\boldsymbol{p}_\alpha = \boldsymbol{d}(\boldsymbol{\rho}_\alpha) - \boldsymbol{d}(\boldsymbol{\rho}_{true}) \tag{3}$$

where, $\boldsymbol{\rho}_\alpha$ is the regularized density vector solution from the algorithm and $\boldsymbol{\rho}_{true}$ is the true density vector. Since the true density is not known, the UPRE, a statistical estimator of $\boldsymbol{p}_\alpha$, was minimized instead. The UPRE was minimized over $\log(\alpha)$ to a tolerance of 0.1.

The algorithm was implemented in Matlab (Mathworks, Inc., Natick, MA).

1. Fuel powder verification measurement

Nuclear fuel powder is produced in fuel fabrication facilities before being sintered into nuclear fuel pellets. This offers an opportunity to inspect a lower-density sample (~3 g/cm^3), where the attenuation around the K-edges of the sample can be observed with typical X-ray radiography systems. In this work it was assumed that the uranium oxide (UO_2) powder to be assayed was placed in a thin-walled plastic or quartz container. The average density of the powder was well below the theoretical density because there was no specific effort made to pack or compact the powder. The density of the simulated UO_2 fuel powders here was 3 g/cm^3, with an option for Gd-loading (Gd_2O_3) of 5 w/o. Fuel powder thicknesses of 1, 3, and 5 mm were simulated to explore if there is an optimal thickness that balances sufficient X-ray transmission and counting statistics with a material thickness sufficient to produce strong contrast in the K-edge signal.

Two types of fuel powder objects were simulated. The first assumes a uniform mixture of fuel powder such that there is no variation in powder density within the object. This offers a best-case with which to compare more realistic simulations. The second object includes more realistic density variation where the density has a 20% or 40% variation around the nominal 3 g/cm^2 density, either normally or uniformly distributed, as shown in Fig. 1 for the 100-117 keV energy window. This simulates the expected variation that could be observed in a loosely tamped powder sample and was simulated by splitting the fuel volume into right parallelepipeds of dimension $0.3 \times 0.1 \times 0.1$ cm^3.

The X-ray source was a cone 300 kVp Bremsstrahlung source with a half-angle of 8.1°, 11 cm from the middle of the inspected object. The source spectrum was simulated in MCNP by transporting electrons onto a tungsten target and tallying the photon production. The X-ray flux was determined from a radiography tally at 20 cm from the middle of the object. The radiography tally was a pixel array of 80 x 80 pixels^2 with 0.1 cm pixel pitch. An example of the radiograph is shown in Fig. 1, for a single energy range on the cadmium telluride detector. Noise was added to these results assuming a maximum count of 10^8 in the background pixels, which corresponds to a data acquisition time of minutes.

The detector response $S_\ell(E)$ in Eq. 1 was modeled in MCNP for a 5-mm thick cadmium telluride detector by tallying the energy deposition in a multi-pixel detector medium. This response $S_\ell(E)$ indicates the probability that an incident X-ray of a given energy will be detected in an energy bin ℓ and shows similarity with experimentally determined response functions [6]. The simulated detector had 6 energy bins, placed to observe the material specific K-edges in the attenuation coefficients μ and the low-energy regions, where μ shows greater uniqueness for varying materials, as shown in Fig. 2. The material attenuation coefficients μ (cm^2/g) were obtained from MCNP, which uses the ENDF cross-section database.

The inverse algorithm requires a set of materials to search for in the data, determined from the user-provided set of material attenuation coefficients μ. This allows flexibility to search for any number of materials in the data, though increasing the number of materials also increases the ill-posedness (instability) of the problem. Nonetheless, accuracy in quantifying three or four materials has been demonstrated previously [4]. Here, a three-material set of {uranium, oxygen, gadolinium} was used for the uniform fuel powder verification measurement, to allow flexibility to possible gadolinium loading, which is typical in nuclear fuel fabrication. For the density varying simulation, a two-material set was used {uranium, oxygen}, which reduces the ill-posedness of the problem. This was done since it was expected that the varying density estimations would present a more difficult problem, though it was subsequently found that a three-material set could also be used here.

Errors on material composition estimated from the algorithm were determined with the relative error e, where the material estimation vector $\boldsymbol{\rho}_{est,k}$ for material k is compared to the true $\boldsymbol{\rho}_{true,k}$.

$$\boldsymbol{e}_k = \frac{\boldsymbol{\rho}_{est,k} - \boldsymbol{\rho}_{true,k}}{\boldsymbol{\rho}_{true,k}} \tag{4}$$

The mean and standard deviation of the $\boldsymbol{e}$ vector are reported as measures of success of the algorithm material estimations. The results include material estimations from 20 independent noise realizations of the image data ignoring a 5-pixel-wide border of the object, to avoid any edge artefacts introduced by the total variation regularization. This results in the $\boldsymbol{e}$ vector containing >34,000 elements (i.e., 20 realizations × 1716 pixels) over which the mean and standard deviations were calculated. When $\boldsymbol{\rho}_{true,k} = \mathbf{0}$, such as when a material estimated from the algorithm was not actually present, the denominator in Eq. (4) was set to 1.

For the object simulations that have density variation, the error reported is on the total mass determined from the algorithm compared to the actual for each material. Here, Eq. (4) was modified to consider the scalar total estimated mass and actual total mass. Notably, the thickness or density of the bulk material need not be assumed for calculation of material mass since the algorithm determines material areal density (g/cm^2), which can be used to calculate the mass directly with a known pixel size and imaging geometry.

2. Verification measurement system variation

Beyond the expected variability in the fuel powder sample density that was introduced in the previous section, it was expected there will be other variabilities in the measurement system, e.g., in the source spectrum or detector response. These variabilities will also affect the estimated material composition since it will affect the accuracy of the detector response $S_\ell(E)$ and input spectrum $\phi_0(E)$ in the forward model, Eq. (1).

Three verification measurement system variations were selected based on what are expected to be the most significant in a deployed system: 1) Bremsstrahlung X-ray spectrum endpoint, 2) energy resolution, as measured by the full-width at half maximum (FWHM), of each detector pixel and 3) detector pixel gain. Examples of these system variations are shown in Fig. 3.

Figure 3a shows how inaccuracy in the Bremsstrahlung X-ray spectrum endpoint will effect the energy spectrum that is used to inspect the object. In particular, an increased endpoint

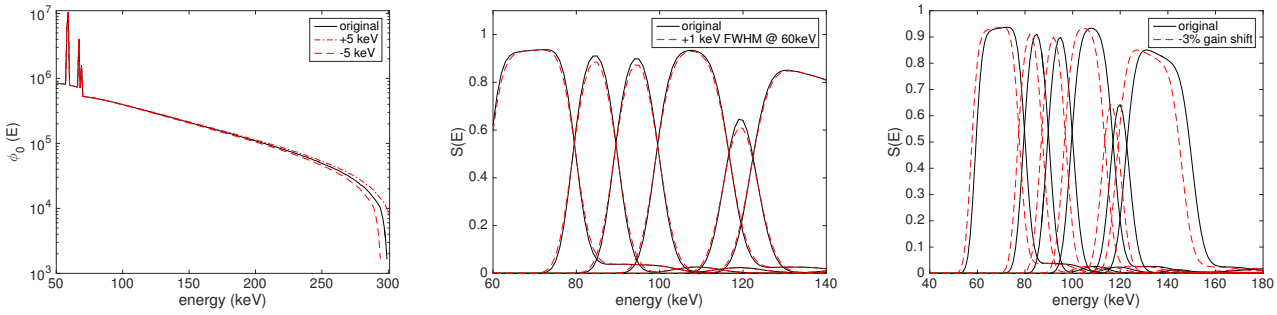

(a) (b) (c)

Fig. 3: Variability in the verification measurement system parameters used to test the sensitivity of the algorithm output to the uncertainty expected in a deployed system. (a) Inaccuracy of the maximum energy of the Bremsstrahlung X-ray beam. (b) Varying detector full-width at half maximum (FWHM) across the detector pixels. (c) Variability in gain across the pixels of the detector.

	Nominal variation
Endpoint energy	1% (~2-3 keV)
Pixel gain	1%
Pixel FWHM	0.4 keV

TABLE I: Approximate variations that could be expected from a typical spectral X-ray verification measurement system.

energy will result in a extension of the energy spectrum that spreads to higher energies, while a decreased endpoint energy will result in a compression of the energy spectrum. These variations cause inaccuracy in the input spectrum $\phi_0(E)$ in Eq. 1.

Two variations in the detector response $S_\ell(E)$ in Eq. (1) were expected to be significant. The first, shown in Fig. 3b, was the pixel FWHM, which will cause sharper energy bin boundaries with lower FWHM. The simulated FWHM also varies with energy such that

$$\text{FWHM}(E) = b + 0.04E \tag{5}$$

where b is defined based on a nominal FWHM, e.g., $b \approx 4.6$ keV for a 7.0 keV FWHM at 60 keV. The second, shown in Fig. 3c, was the pixel gain, which will extend or compress the energy bins on the detector due to an over or underestimate on the gain, respectively. Notably, both the pixel gain and pixel FWHM can vary across the pixels of the detector so that the gain or FWHM may not be the same between neighboring pixels.

The level of these variations expected in the measurement system, based on device documentation and literature [9, 10], are shown in Table I.

In order to test the sensitivity of the inverse algorithm to these expected variations, the algorithm was run with various levels of variation in the Bremsstrahlung spectrum and detector response. Regarding the variation in the Bremsstrahlung spectrum, this was done by shifting the spectrum endpoint according to a sample from a normal distribution with mean 300 keV and some defined standard deviation. This spectrum shift affects all pixels on the detector in the same way. In contrast, the detector response may vary from one pixel to the next. Therefore, the variation in detector gain and FWHM was simulated by sampling these parameters pixel-by-pixel from a normal distribution with 0 mean and few standard deviations near those shown in Table I.

In order to isolate the sensitivity to each given measurement system variation, the simulated measurement case used for these studies was the 3-mm thick UO_2 fuel density, without image noise. A two-material set {uranium, oxygen} was used here. The sensitivities were tested with $\alpha = 10^{3.7}$, which was found to be optimal according to the UPRE parameter selection method.

III. RESULTS AND ANALYSIS

Results from the inverse algorithm are shown in Fig. 4 for the uniform 3-mm material thickness and the relative error of the estimations, Eq. (4), are summarized in Table II. The results show bias on the mean estimated uranium content of $\leq 0.01\%$ with a standard deviation of $< 0.1\%$ for all cases. Importantly, the algorithm can also determine gadolinium (Gd) content directly with a minimal impact on the uranium accuracy, allowing greater flexibility for measurement of typical fuel compositions.

Results from the variable density simulations are shown in Fig. 5 for the 20% normally distributed and 40% uniformly distributed density cases. These results are also summarized in Table III. Here, the relative error was reported on the total mass determined from the algorithm compared to the true value in the simulated sample. The effective mass can be calculated from the algorithm output by multiplying the pixel-wise material estimations in g/cm^2 by the area projected in the sample plane on the detector plane. Given the simulated image geometry in this work the 0.1×0.1 cm^2 pixel area was 0.038×0.038 cm^2 in the object plane. Note, since the object has a finite thickness of 0.3 cm this projected area was the average of the projected area from the front and back of the fuel powder volume.

	e_U (%)	e_O (%)	e_{Gd} (%)
UO_2 3-mm	0.00 ± 0.04	-0.89 ± 4.88	0.01 ± 0.01
UO_2 3-mm, with Gd	0.01 ± 0.05	-0.48 ± 5.60	0.01 ± 0.58
UO_2 1-mm	-0.01 ± 0.05	-0.25 ± 6.42	0.00 ± 0.01
UO_2 5-mm	0.01 ± 0.07	-2.76 ± 7.03	0.02 ± 0.04

TABLE II: Relative error (e) on material estimations for simulated measurements of samples assumed to have uniform density.

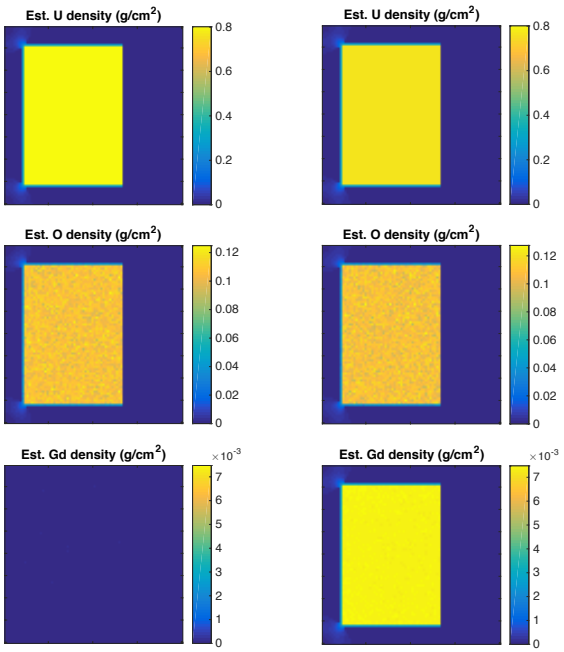

(a) (b)

Fig. 4: Material estimations from the uniform 3 g/cm^3, 3-mm thick fuel powder verification measurement without (a) and with (b) Gd loading of 5 w/o. Accuracies are summarized in Table II.

The results show bias on the mean estimated uranium mass of less than 0.2% with a standard deviation of less than 0.002%, even with a large density deviation of 40%. The 40% density variation may overestimate that which will be seen in practice. The bias on the material estimation was likely due to the X-rays passing through multiple material density voxels, as they may be approaching the sample at some small angle, due to the divergence of the beam. Also, the standard deviation was lower here since the mass result is essentially a sum of the density estimations from a number of pixels, effectively cancelling out the positive and negative variations seen in the material estimations from pixel to pixel.

Sensitivity of the estimated uranium estimation with respect to variations in the measurement system are shown in Table IV. The variation levels shown are the mean and standard deviation of the normal distribution sampled to simulate the given variation. The uranium error mean and standard deviations quantify both the bias and degradation in precision of the measurement from these system variations.

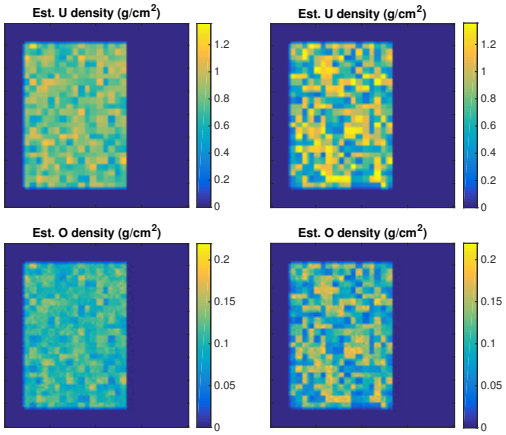

(a) (b)

Fig. 5: Material estimations from the UO_2 fuel sample with density variation of (a) 20% normally distributed and (b) 40% uniformly distributed. The results are summarized in Table III.

Density distribution	Estimated U mass error (%)
20% normal	0.068 ± 0.001
20% uniform	0.086 ± 0.001
40% uniform	0.182 ± 0.001

TABLE III: Relative error on total uranium mass using simulations with varying density.

Biases, indicated by the mean relative error, caused by variation in the spectrum endpoint and pixel FWHM were minimal, while the bias caused by variation in the pixel gain was significant, though still less than 1%. The bias on gain shifting was likely due to the energy bins surrounding the uranium attenuation coefficient K-edge, e.g., Fig. 2. Negative gain shifts will cause greater uranium underestimation than the uranium overestimation caused by positive gain shifts, due to the asymmetric energy bin size on either side of the K-edge. This could be mitigated with a different energy bin structure.

Apart from the effect on the bias, the results also indicate a reduction in uranium estimate precision with measurement system variations, indicated by the standard deviation of the uranium relative error. The results show that precision was not significantly degraded with variation in the pixel FWHM, though precision was degraded with variation in the spectrum endpoint and especially so with variation in the pixel gain. This lines up with expectations since the inverse algorithm

Variation	Level	e_U (%)
Spectrum endpoint	300 ± 2 keV	0.01 ± 0.23
	300 ± 3 keV	0.01 ± 0.35
Pixel FWHM	7.0 ± 0.4 @ 60 keV	0.00 ± 0.04
	7.0 ± 0.8 @ 60 keV	−0.03 ± 0.09
Pixel gain	1.0 ± 0.005	−0.18 ± 0.93
	1.0 ± 0.01	−0.6 ± 1.8

TABLE IV: The sensitivity of the uranium (U) estimated from the algorithm to variations in the measurement system.

relies on spectral information to estimate material composition. Any shift in that spectral information, either from the source or the detector, will affect the material estimations. Variation in pixel gain, again, was shown to especially affect the material estimations since shifts of the energy bins will significantly affect the spectral information acquired on the detector, e.g., Fig. 3c. Spectral shifts around the attenuation coefficient K-edges, on which much of the uranium quantification depends, cause a significant effect.

It should be noted that these sensitivity results assumed that the detector response function $S_\ell(E)$ for each pixel on the detector was not fully known. For any one of these measurement system variations, a full characterization of the detector response that captures these pixel-to-pixel variations reduces the relative error values to those shown in Table II. Furthermore, the use case for this technology is to quantify uranium content in the entire sample, which effectively means taking an average of uranium estimations across many pixels. This means that biases in the results are more important than the precision.

The biases observed in the sample density variation and detector gain variation indicate that these variations should be mitigated in an measurement system design, wherever possible. This can be accomplished with careful sample preparation and accurate, pixel-by-pixel, detector response characterization, respectively.

IV. CONCLUSIONS

Using simulated data and a flexible, adaptive inverse algorithm, we have preliminarily explored the feasibility of using spectral X-ray radiography to perform nondestructive verification measurements on fuel powder samples in fuel fabrication facilities. Material composition was estimated in the algorithm, which can be directly related to material mass by using known assay-system and sample-geometry parameters. Initial findings on the achievable accuracy and precision of this spectral X-ray method indicate strong potential to meet or exceed IAEA's target for the assay of uranium oxide samples in the field (0.28%). Importantly, the method introduced here offers nondestructive assay in a fraction of the time required by the current IAEA methods, and requires no on-site chemistry work or specialized user expertise.

In order to simulate the expected variations that will be seen in a deployed verification measurement system, system parameters of interest were varied and resulting algorithm accuracy and precision were reported. Variations in the system that were studied were: sample density inhomogeneity, X-ray source endpoint, detector response FWHM, and detector response gain. It was found that the algorithm is most sensitive to sample powder density variation and detector response gain. In practice, these effects could be mitigated through measurement system design; by limiting sample powder variation (e.g., by tamping the powder in the holding container) and by determining to high-accuracy, the pixel-by-pixel gain variation. Importantly, a well characterized measurement system and detector response will result in the highest accuracy material estimations.

While the results presented here are encouraging, it remains to be seen how well the an experimental system will perform. From the sensitivity studies presented here, it appears that the biases and standard deviations on the material estimations caused by system variations are relatively small, indicating the feasibility of the measurement system for non-invasive nuclear fuel powder quantification under IAEA safeguards. To this end, verification measurement system design and optimization is underway, as is acquisition of spectral X-ray data with an experimental measurement system.

V. ACKNOWLEDGMENTS

The authors wish to thank Jon Kulisek for aiding in the generation of the radiography simulations. This research was sponsored by Pacific Northwest National Lab, Laboratory Directed Research and Development (LDRD). This research was supported in part by the U.S. National Nuclear Security Administration (NNSA) Office of Nonproliferation and Arms Control (NPAC) within the U.S. Department of Energy (DOE) under Contract DE-AC05-76RL01830. A. J. Gilbert is supported by NPAC, Office of International Nuclear Safeguards Human Capital Development program. A portion of this research was performed using PNNL Institutional Computing at Pacific Northwest National Laboratory. The external release identifier for this publication is PNNL-SA-124031.

REFERENCES

1. A. BERLIZOV, A. SCHACHINGER, K. ROETSCH, N. ERDMANN, H. SCHORLÉ, M. VARGAS, J. ZSIGRAI, A. KULKO, M. KESELICA, F. CAILLOU, V. UNSAL, and A. WALCZAK-TYPKE, "Feedback from operational experience of on-site deployment of bias defect analysis with COMPUCEA," *Journal of Radioanalytical and Nuclear Chemistry*, pp. 1–9 (2015).
2. "ORTEC Hybrid K-Edge Densitometer," www.ortec-online.com/download/hked.pdf (2016).
3. A. J. GILBERT, B. S. MCDONALD, and M. R. DEINERT, "Advanced algorithms for radiographic material discrimination and inspection system design," *Nuclear Instruments and Methods in Physics Research Section B*, **385**, 51–58 (2016).
4. A. J. GILBERT, B. S. MCDONALD, S. M. ROBINSON, K. D. JARMAN, T. A. WHITE, and M. R. DEINERT, "Non-invasive material discrimination using spectral x-ray radiography," *Journal of Applied Physics*, **115**, *15* (2014).

5. MCNP X-5 MONTE CARLO TEAM, "A General Purpose Monte Carlo N-Particle Transport Code," (2003).
6. J. P. SCHLOMKA, E. ROESSL, R. DORSCHEID, S. DILL, G. MARTENS, T. ISTEL, C. BÄUMER, C. HERRMANN, R. STEADMAN, G. ZEITLER, A. LIVNE, and R. PROKSA, "Experimental feasibility of multi-energy photon-counting K-edge imaging in preclinical computed tomography," *Physics in Medicine and Biology*, **53**, *15*, 4031 (2008).
7. J. M. BARDSLEY and J. GOLDES, "Regularization parameter selection methods for ill-posed Poisson maximum likelihood estimation," *Inverse Problems*, **25**, *9*, 095005 (2009).
8. C. R. VOGEL, *Computational Methods for Inverse Problems*, SIAM, Philadelphia (2002).
9. A. MATTNER, *Comet XRP Generator User Manual*.
10. M. C. VEALE, S. J. BELL, D. D. DUARTE, A. SCHNEIDER, P. SELLER, M. D. WILSON, and K. INIEWSKI, "Measurements of charge sharing in small pixel CdTe detectors," *Nuclear Instruments and Methods in Physics Research Section A: Accelerators, Spectrometers, Detectors and Associated Equipment*, **767**, 218–226 (2014).